Journal of Materials Chemistry

Cite this: *J. Mater. Chem.*, 2012, **22**, 15316

www.rsc.org/materials

PAPER

Alternately deposited heterostructures of α-sexithiophene–*para*-hexaphenyl on muscovite mica(001) surfaces: crystallographic structure and morphology

Tatjana Djuric,*[a] Gerardo Hernandez-Sosa,[b] Günther Schwabegger,[b] Markus Koini,[a] Günter Hesser,[c] Martin Arndt,[c] Martin Brinkmann,[d] Helmut Sitter,[b] Clemens Simbrunner[b] and Roland Resel[a]

Received 31st March 2012, Accepted 25th May 2012
DOI: 10.1039/c2jm32023a

Multi-component systems of *para*-hexaphenyl (*p*-6P) and α-sexithiophene (α-6T) molecules show great promise for tuning the fluorescence colour of optically active films. As the opto-electronic properties of rod-like molecules in thin films strongly rely on their anisotropic orientation, a technique for preparation of well-defined, anisotropic multicomponent systems is required. We demonstrate that a *p*-6P film of less than two nanometer thickness grown on muscovite mica(001) substrates acts as an efficient alignment layer for epitaxial growth of α-6T crystallites. On top of such a *p*-6P alignment layer, multilayer heterostructures of alternately deposited *p*-6P and α-6T molecules were grown. Combined X-ray diffraction and transmission electron microscopy studies show that molecules forming α-6T crystallites align parallel to those in the *p*-6P crystallites leading to the perfect adoption of their herring-bone structures. This alignment is desirable for optical applications and we show that it is preserved for heterostructures composed of up to 120 alternately deposited *p*-6P (0.8 nm) and α-6T (3.4 nm) nominal layers (120 cycles). Although for co-evaporated α-6T–*p*-6P molecules formation of a mixed crystal polymorph is reported, we show that in periodically deposited α-6T–*p*-6P heterostructures phase separation occurs and both molecules crystallize in their well-known equilibrium structures.

1 Introduction

para-Hexaphenyl (*p*-6P, $C_{36}H_{26}$) and α-sexithiophene (α-6T, $C_{24}H_{14}S_6$) are amongst the most important rod-like molecules intended for applications in organic semiconductor devices like organic light-emitting devices (OLEDs)[1–3] and organic field-effect transistors (OFETs).[4–6] As their optical transition dipole moments are oriented along the long molecular axes, for applications as optically active materials well-ordered films of parallel aligned molecules are required.[7,8]

Highly ordered *p*-6P thin films can be obtained by epitaxial growth on muscovite mica(001) surfaces.[9,10] When deposited on a muscovite mica(001) surface *p*-6P molecules first form a closed monolayer of flat lying molecules.[11] Subsequently formed crystallites arrange epitaxially to long (μm range) and highly ordered self-assembled needles.[10,12,13] *para*-Hexaphenyl molecules forming highly anisotropic needles show a high quantum yield in the blue spectral regime[14] and, more remarkably, the elongated shape of the needles enables wave guiding and lasing.[15,16] Due to the structural similarity between *p*-6P and α-6T, muscovite mica(001) substrates were considered as favourable templates for the growth of α-sexithiophene thin films as well.[17–19] However, morphological and structural studies have shown that – although α-6T molecules tend to arrange in needle-like structures on muscovite mica(001) surfaces – their epitaxial alignment is much more complicated.[18,20] They show multi-directional azimuthal alignment which is strongly disadvantageous for the formation of long nano-fibres and thus suppresses waveguiding and lasing.

Classical inorganic–organic heteroepitaxy is extensively utilized for the growth of anisotropic crystalline organic films. It was only recently that the potential of organic–organic heteroepitaxy was recognized.[21–25] Koller *et al.* (2006) have shown that the approach of organic–organic heteroepitaxial growth of *p*-6P and α-6T molecules enables the growth of thin films with high crystallinity and well-defined interfaces, thus meeting the requirements for applications as active materials in organic semiconductor devices.[24] In addition to that, organic–organic heteroepitaxy enables adjustment of the physical properties of the organic multilayers as well. In particular, for α-6T–*p*-6P bilayers on muscovite mica(001) surfaces Simbrunner *et al.* (2010)[25] have shown that an α-6T layer deposited on top of a *p*-6P layer changes the emission color from blue to green. Furthermore, through the deposition on highly ordered *p*-6P template fibres the multiple azimuthal orientations of α-6T needles – as observed on bare mica(001) substrates – are suppressed. Due to the anisotropic molecular alignment of *p*-6P as well as of α-6T crystallites, highly polarised fluorescence in the green range is observed.

[a]*Institute of Solid States Physics, Graz University of Technology, Austria. E-mail: tatjana.djuric@gmx.net*
[b]*Institute of Semiconductor and Solid State Physics, Johannes Kepler University, Linz, Austria*
[c]*ZONA (Zentrum f. Oberflächen- und Nanoanalytik), Johannes Kepler University, Linz, Austria*
[d]*Institut Charles Sadron, CNRS - Université de Strasbourg, France*

In order to obtain a more precise tuning of the emission chromaticity of α-6T–*p*-6P nanofibers the heteroepitaxy bilayer approach was extended to a system of periodically, *i.e.* alternately, deposited α-6T and *p*-6P layers grown on top of a *p*-6P template layer.[26] In this work, we focus on the structure and morphology of such alternately deposited α-6T–*p*-6P heterostructures grown by hot-wall epitaxy (HWE). For high optical efficiency in such heterostructures it is crucial that the epitaxial alignment of molecules parallel to each other is preserved. Therefore, it is important to investigate how the periodical deposition influences the crystallization behaviour of the two molecular species. Beside the entropy term, also the particular intermolecular interactions determine whether a regular solution (random mixing), ordered mixed crystal (solid solution) or phase separation will occur.[27–31] Generally, unless the mixed molecules show a high degree of structural compatibility, phase separation is expected when two molecular compounds are mixed.[32,33] In principle, α-6T and *p*-6P molecules comply with the requirements for building mixed crystals: they are of similar size (van der Waals length of 2.61 nm (α-6T) and 2.87 nm (*p*-6P)) and in equilibrium they form the same type of crystal structure (monoclinic, space group 14) with a herring-bone packing.[5,34] Moreover, for co-evaporated α-6T–*p*-6P heterostructures Vogel *et al.* (2010)[35] have demonstrated that they indeed form mixed crystals and that the length difference between the two molecules is crucial for their mixing behaviour. The smaller α-6T molecules are integrated into a crystal network of the larger *p*-6P molecules forming a mixed crystal with an intermediate interlayer spacing; the opposite scenario is not observed. In particular, it is of interest to observe how the structural properties of the films prepared by alternate deposition of *p*-6P and α-6T layers by hot wall epitaxy differ from the corresponding films obtained by co-evaporation of both molecules.

Using X-ray diffraction (XRD), transmission electron microscopy/diffraction (TEM/TED), Auger electron spectroscopy (AES) and atomic force microscopy (AFM) the crystallization behaviour of periodically deposited α-6T–*p*-6P organic–organic heterostructures is investigated. By combining these methods the evolving crystallographic phases, the arrangement of molecules relative to each other as well as the resulting morphology of the films are determined.

2 Experimental

The samples were prepared by hot wall epitaxy (HWE) operated under high vacuum conditions with a nominal pressure of 9×10^{-6} mbar. Cleaved muscovite mica(001) (SPI, Structure Probe, Inc.) substrates were transferred *via* load lock to the growth chamber and were preheated at the chosen substrate temperature T_{sub} (90 °C/120 °C) for 30 min. This step cleans the surface and helps to avoid temperature gradients during the growth. The used compounds *p*-6P (TCl) and α-6T (Sigma-Aldrich) were placed in two separated reactors in the growth chamber (see Fig. 1). The optimized evaporation temperature for the source materials *p*-6P (α-6T) is found at $T_{source} = 240$ °C (190 °C). The wall temperature is set to $T_{wall} = 260$ °C. The selected growth parameters lead to a nominal growth rate of 3.27 nm min^{-1} (4.5 nm min^{-1}). The nominal thickness used in this article is defined as the average fibre height. As the fibres do not cover the whole surface a definition of the growth rate in terms of a full layer coverage is not preferable. Consequently, the growth rate has been defined in terms of the increasing fibre height per minute. Values have been deduced from height histograms obtained by AFM analysis (for *p*-6P and α-6T grown separately on mica). For the growth of α-6T molecules on *p*-6P template layers T_{sub} was set to 90 °C or 120 °C, respectively. For the fabrication of periodically grown heterostructures $T_{sub} = 120$ °C was selected. The first step in the preparation of the periodically grown samples is the deposition of a *p*-6P template layer for 10 min (~32.7 nm). Subsequently, the periodical deposition of *p*-6P and α-6T molecules is initialized. The repetition unit of one *p*-6P and one α-6T layer in the subsequently initialized periodic deposition is denoted a *deposition cycle*. In this study, samples prepared with 0, 1, 10, 30, 75 and 120 cycles are discussed. The total nominal thickness of the deposited material t_{total} as well as the total thicknesses of the two molecular species is constant for all samples ($t_{total} = t_{total,6P} + t_{total,6T}$, *p*-6P: $t_{total,6P} = 98.1$ nm, α-6T: $t_{total,6T} = 405$ nm). Accordingly, the nominal thickness grown in a *single* cycle depends on the total number of deposition cycles (see Table 1).

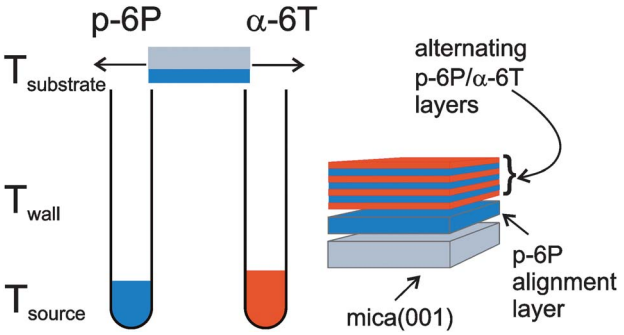

Fig. 1 Sketch illustrating the deposition of alternating α-6T–*p*-6P layers on a muscovite mica(001) substrate using the hot wall epitaxy system equipped with two separated growth reactors.

X-ray diffraction specular scans and reciprocal space maps (RSMs) were measured on a Bruker D8 Discover diffractometer in the Bragg–Brentano configuration using CuKα radiation ($\lambda = 1.54$ Å). RSMs provide a two-dimensional cross-section of the reciprocal space (here in q_x and q_z). The variation along the q_z-direction at $q_x = 0$ corresponds to a specular scan, *i.e.* to Bragg peaks of lattice planes exactly parallel to the sample surface. The variation along q_x for a constant $|\boldsymbol{q}|$-value ($|\mathbf{q}| = \sqrt{q_x^2 + q_z^2}$) is

Table 1 Nominal thicknesses of *p*-6P (t_{6P}) and α-6T (t_{6T}) layers deposited in a single cycle at $T_{sub} = 120$ °C on a 33 nm thick *p*-6P template layer. The total thickness of the formed multilayer heterostructures is kept constant: $t_{total,6P} = 98.1$ nm and $t_{total,6T} = 405$ nm

Number of cycles	t_{6P}/nm	t_{6T}/nm
0	98.1	—
1	98.1	405
10	9.8	40.0
30	3.3	13.5
75	1.3	5.6
120	0.8	3.4

equivalent to rocking curves indicating the mosaicity of the crystallites, *i.e.* for a given Bragg peak it is representative of the tilting of the corresponding lattice planes relative to the substrate. The diffractometer was equipped with conventional slit optics and a graphite monochromator on the secondary side. Pole figure measurements were performed on a Philips X'Pert X-ray diffractometer with CrKα radiation ($\lambda = 2.29$ Å). For the assignment of Bragg peak position POWDER CELL[36] was used and the simulation of the pole figure measurements was done with STEREOPOLE.[37] The *p*-6P crystallites were assigned to the β-crystal structure with the following unit cell parameters: $a = 8.8091$ Å, $b = 5.5680$ Å, $c = 26.2410$ Å and $\beta = 98.17$.[34] α-6T molecules exhibit the so-called low temperature phase with $a = 44.708$ Å, $b = 7.851$ Å, $c = 6.029$ Å and $\beta = 90.76°$.[5]

For transmission electron microscopy/diffraction (TEM/TED) measurements carbon coated samples were removed from the muscovite mica substrate by floating on a dilute HF (hydrofluoric acid) solution and were subsequently recovered on copper TEM grids. TEM investigations were performed in bright field (BF) and selected area electron diffraction (SAED) modes using a Philips CM12 microscope (120 kV) equipped with a MVIII CCD camera. Calculation of the electron diffraction (ED) patterns was carried out using the program Cerius² (Accelrys).

Atomic force microscopy (AFM) studies of the deposited nano-fibres were performed using a Digital Instruments Dimension 3100 in the tapping mode. The AFM characterization was performed on an area of 30 μm² with a SiC tip. The pixel resolution was chosen with 512 × 512 pixels. The zero height has been corrected by levelling the data to the minimum height of the whole image.

Cross-sectional TEM measurements were carried out on a JEOL 2011 microscope (200 kV, LaB_6) attached with an OXFORD EDX-System for elemental analysis. Sample preparation with the focused ion beam technique was carried out using a ZEISS XB 1540 Crossbeam after depositing an aluminium layer for protection and anti-charging purposes by thermal deposition. The Auger images were taken at a tilt angle of 30° to the 30 kV primary electron beam and 30° to the concentric hemispherical analyzer (CHA) as a good compromise between distortion and count rate. The primary electron beam current was set to 10 nA. Each Auger image consists of 128 × 128 pixels with a dwell time of 50 ms per pixel. For the C image the KLL Auger peak at 263 eV and for the S mapping the LVV Auger peak at 146 eV were used, respectively.

3 Results

3.1 Growth of α-6T molecules on *p*-6P template layers

Before turning to the central topic of this article (alternately deposited α-6T–*p*-6P heterostructures), we investigate the influence of the *p*-6P alignment layers on the subsequently deposited α-6T molecules in a simple bilayer system. The role of the template layer thickness on the alignment of the α-6T molecules is investigated, an issue not discussed in the recently published results on bilayer α-6T–*p*-6P nano-fibers.[25] Further on, TEM/TED measurements of a bilayer system are presented which are subsequently used as a reference system for the periodically deposited α-6T–*p*-6P heterostructures.

AFM measurements summarized in Fig. 2 show that already very thin layers of *p*-6P act as efficient templates for the alignment of subsequently deposited α-6T molecules ($t_{6T} = 45$ min, 200 nm). When deposited on an only 0.3 nm thick *p*-6P template layer (corresponds to one monolayer)[11] grown at $T_{sub} = 90$ °C α-6T molecules arrange in needle-like aggregates but still show a strongly pronounced multidirectionality (Fig. 2a). However, a template thickness of 1.6 nm (Fig. 2b) is already sufficient to significantly reduce the branching of the α-6T needles. Also samples prepared at an elevated substrate temperature ($T_{sub} = 120$ °C) were investigated and we observe that the directionality of the α-6T needles is further improved (Fig. 2c). This is in line with the general observation that the morphology of (template) fibres improves with increasing substrate temperature.[38] Moreover, we find that an increased thickness of the *p*-6P template layer (which is not directly observed by AFM) also remarkably increases the nucleation density of the α-6T needles (Fig. 2d).

To demonstrate that a *p*-6P template layer with a thickness of 1.6 nm is sufficient to induce high azimuthal anisotropy of the subsequently deposited α-6T molecules, the morphology as well as the crystallographic properties of these films were investigated in detail by TEM and TED in high resolution. A representative α-6T thin film grown on a 1.6 nm thick *p*-6P template at $T_{sub} = 90$ °C (see Fig. 2b) is discussed here. Besides the long branched α-6T needles (length: 10–30 μm, width: 0.1–0.3 μm) which were already observed in Fig. 2, TEM bright field images additionally reveal elongated islands (Fig. 3a). Their dimensions are uniformly distributed with a typical length of approximately 50 nm and a width of 20 nm. Fig. 3b shows that α-6T needles align nearly parallel to these elongated islands.

Pure *p*-6P films prepared with comparable growth time ($t_{6P} = 26$ s) at the same $T_{sub} = 90$ °C have shown a uniform coverage

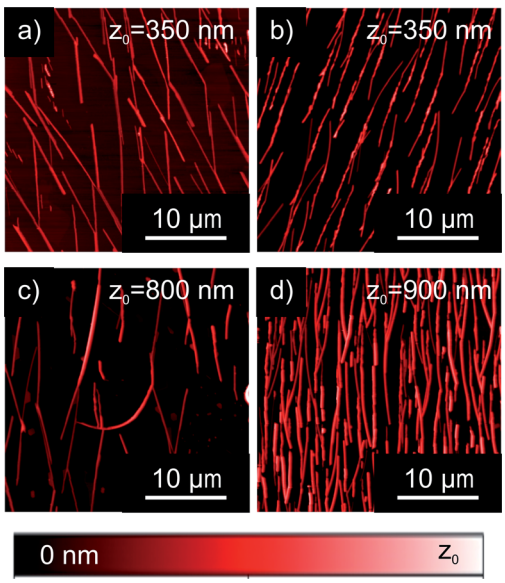

Fig. 2 AFM measurements of α-sexithiophene needles (nominal thickness $t_{6T} = 200$ nm) grown on *p*-hexaphenyl covered muscovite mica(001) surfaces. Underlying *p*-hexaphenyl template layers were prepared at different substrate temperatures T_{sub} and nominal thicknesses t_{6P}: (a) $T_{sub} = 90$ °C, $t_{6P} = 0.3$ nm, (b) $T_{sub} = 90$ °C, $t_{6P} = 1.6$ nm, (c) $T_{sub} = 120$ °C, $t_{6P} = 0.3$ nm and (d) $T_{sub} = 120$ °C, $t_{6P} = 1.6$ nm.

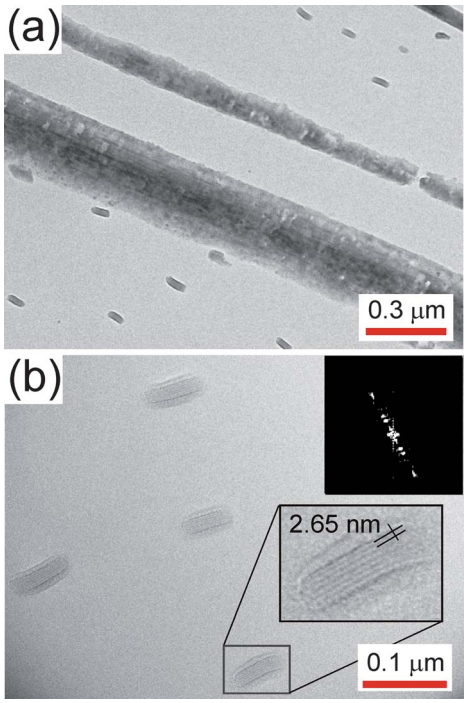

Fig. 3 (a) TEM bright field image of a 200 nm thick α-6T film grown on a 1.6 nm thick *p*-6P template layer. (b) High-resolution TEM image of *p*-6P elongated islands. The inset in the right corner shows a fast Fourier transform of a single island.

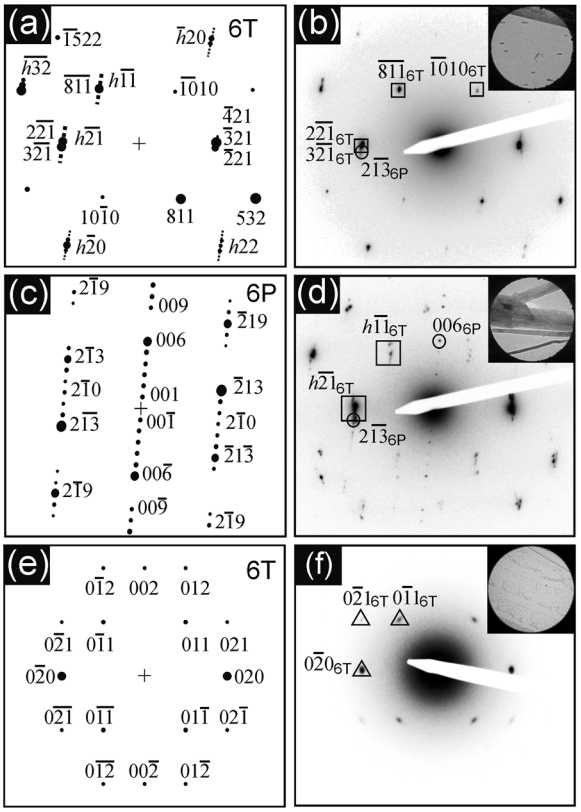

Fig. 4 The left column shows calculated electron diffraction (ED) patterns: (a) for the low temperature phase of α-6T assuming a $[\bar{3}.\bar{2}\bar{5}.42]$ zone axis (corresponding to rectangles in the right column), (c) for the β-phase of *p*-6P assuming the [120] zone axis (corresponding to circles in the right column) and (e) for the low temperature phase of α-6T assuming a [100] zone axis (corresponding to triangles in the right column). The right column shows measured diffraction patterns for a 200 nm thick α-6T film grown on a 1.6 nm thick *p*-6P template layer with indexed reflexes. The insets show the corresponding defocused image of the diffracting area.

with elongated islands of similar dimensions.[10] They were reported to crystallize in the β-structure of *p*-6P[34] with the $(11\bar{1})$ lattice planes aligned parallel to the muscovite mica(001) substrate surface (contact plane). This orientation corresponds to nearly flat lying molecules. Hence, the morphology observed in Fig. 3 is already a first hint that elongated islands are composed of *p*-6P crystallites exhibiting preferentially the $(11\bar{1})$ contact plane. For further examination, high-resolution images (HR-TEM) of such elongated islands were taken. The Fourier Transform (FT) of a single island (see inset of Fig. 3b) reveals a periodicity of about 2.65 nm which is in good agreement with the (001) spacing of the *p*-6P crystal structure (d_{001} = 2.60 nm) and corroborates that the elongated islands are indeed composed of *p*-6P molecules with the $(11\bar{1})$ contact plane parallel to the substrate.

Fig. 4 summarizes representative electron diffraction (ED) patterns observed for the sample shown in Fig. 2b. Calculated patterns are shown in the left column; they are individually or collectively present in the measured diffraction patterns shown in the right column. Fig. 4b shows an exemplary simple diffraction pattern originating from the edge of the large needle seen in the defocused SAED image in the inset. The diffraction pattern depicted in Fig. 4a was in a first step calculated using the low temperature crystal structure of α-6T[5] assuming the $[\bar{3}.\bar{2}\bar{5}.42]$ zone axis (alignment of the $(\bar{4}11)$ lattice plane parallel to the substrate surface). Depending on the tilt from this assumed zone axis, different reflexes appear (indicated by dashed lines in Fig. 4a) for the two strong series $(h\bar{1}\bar{1})$ and $(h\bar{2}\bar{1})$. Perfect agreement (Fig. 4b) with the measured pattern was obtained here by tilting the assumed zone axis by 3.8° (tilt axis oriented in a direction perpendicular to the direction of the $(\bar{3}21)$ reflection), indicating that the orientation of the crystallite is slightly tilted with respect to the $(\bar{4}11)$ lattice plane.† This orientation implies that the long molecular axis (LMA) of α-6T molecules is nearly parallel to the substrate surface.

In addition to the edge of a thick needle also few elongated islands are present in the area shown in the inset. As their scattering volume is rather small the contribution to the diffraction pattern is rather weak. Fig. 4d shows an ED pattern where domains with slightly varying tilts from the $(\bar{4}11)$ lattice plane are contributing (marked by rectangles); their positions lie along the dashed line shown in Fig. 4a. The diffraction spots marked by circles are stemming from the *p*-6P$(11\bar{1})$ crystallites (compare with the calculated pattern in Fig. 4c). Here, diffraction spots of both molecular species are present, enabling a determination of their relative azimuthal orientation. Generally in an ED pattern, lattice planes perpendicular to the contact plane are visible. Here, we observe that in-plane the $(3\bar{2}\bar{1})$ lattice plane of α-6T

† The bending of the TEM grid can cause a tilt of the contact plane with respect to the electron beam as well.

crystallites has arranged nearly parallel to the $(2\bar{1}\bar{3})$ lattice plane of *p*-6P crystallites. Both lattice planes are parallel to the edge-on molecules in the corresponding crystal structures and they have a similar lattice spacing: $d_{3\bar{2}\bar{1}} = 3.217$ Å for α-6T and $d_{2\bar{1}\bar{3}} = 3.116$ Å for *p*-6P. Their alignment parallel to each other has the effect that α-6T crystallites perfectly adopt the herring-bone structure of the *p*-6P crystallites with both molecular species showing identical orientation (see Fig. 5).

Fig. 4f finally shows a diffraction pattern which is measured only in few regions on the sample. It shows a perfect agreement with the theoretical pattern (Fig. 4e) calculated using the low temperature phase of α-6T and assuming the [100] zone axis (corresponds roughly to the (100) contact plane). α-6T crystallites exhibiting this contact plane are formed by molecules which are nearly perpendicular to the substrate surface. The corresponding morphology shown in the defocused SAED (inset) exhibits rather low contrast indicating small thicknesses in this area. Such islands of upright α-6T molecules are frequently observed on muscovite mica(001) substrates.[17,18,20,39] As the diffraction pattern as well as the defocused selected area image does not indicate underlying *p*-6P elongated islands, the upright α-6T molecules are most probably growing directly on the muscovite mica substrate surface. To summarize the orientations of the crystallites found in α-6T thin films grown on *p*-6P template layers: elongated islands of *p*-6P$(11\bar{1})$ crystallites induce epitaxial growth of needle-like α-6T$(\bar{4}11)$ crystallites (Fig. 5). In between these needle-like structures also a population of α-6T(100) crystallites corresponding to standing molecules are observed which most probably grow directly on the substrate.

3.2 Periodic α-6T–*p*-6P multilayer heterostructures

For bilayer systems of *p*-6P and α-6T molecules showing high azimuthal anisotropy a shift in the spectral emission from blue to green was demonstrated.[25] More precise tuning of the emission chromaticity is possible using a modified hetero-epitaxy approach where α-6T and *p*-6P molecules are deposited alternately on top of each other (on top of a *p*-6P template layer on muscovite mica).[26] To obtain well-defined and densely packed thin films a substrate temperature of $T_{sub} = 120$ °C was chosen (see Fig. 2). As shown, the thickness of the *p*-6P alignment layer does not play a major role in the alignment of 6T$(\bar{4}11)$ crystallites; here, we are using a 33 nm thick *p*-6P template layer to avoid the formation of 6T(100) crystallites. The preparation of such heterostructures is schematically shown in Fig. 1 and explained in detail in the Experimental section. Samples prepared by deposition cycles as listed in Table 1 were investigated.

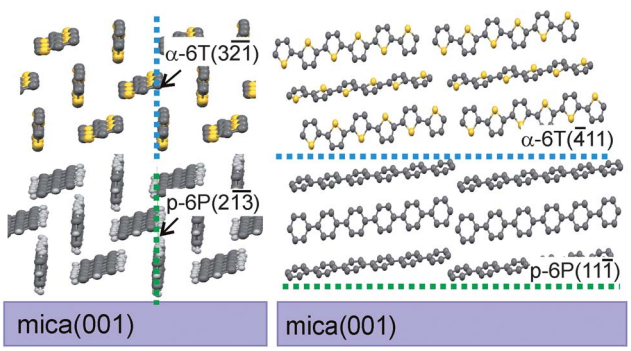

Fig. 5 Molecules as arranged in *p*-6P–α-6T heterostructures on the muscovite mica(001) substrate. On top of the *p*-6P layer α-6T crystallites are formed. In the left panel the view along the long molecular axis, in the right panel perpendicular to it is shown.

For these systems to be useful for optical applications it is essential to preserve the epitaxial alignment observed in bilayer systems (Fig. 5). Therefore, it is of interest to investigate if the periodical deposition affects the crystallization behaviour of the two molecules. It is known that aromatic molecules often form solid solutions (mixed crystals).[33,40,41] Due to the high structural compatibility of the respective molecules (see Introduction), a formation of solid solutions is a plausible scenario as well. Most commonly, substitutional solid solutions are formed, where molecules of the one kind replace molecules of the other kind and occupy exactly the same crystal site.[40] The effect of such a substitution on the newly formed crystal structure can be phenomenologically described by Vegard's law: the new lattice constants are the weighted (by concentration) average of the lattice constants of its components.[33] Also so-called "structural mimicry"[42] is observed, where the lattice constants of the formed mixed crystal do not change as the minor component adopts the structure of the dominant one.[42–44] If no solid solution is formed at all, molecules either crystallize in separate phases or form an amorphous phase.

Therefore, when investigating the structural properties of periodically deposited α-6T–*p*-6P heterostructures, the following questions arise: (a) Is the azimuthal alignment of the *p*-6P–α-6T crystallites preserved? (b) Does the number of deposition cycles have an influence on the epitaxial alignment of the formed crystallites? and finally (c) Do the two components mix on the molecular level and form solid solutions?

3.2.1 TEM/TED measurements. Fig. 6 summarizes TEM and TED measurements performed on a 1-cycle sample (left column) and on a 120-cycle sample (right column). The diffraction pattern measured for the 1-cycle sample shown top left is basically identical to the one obtained for the α-6T film grown on a *p*-6P monolayer (Fig. 4d). It yields the information that both molecules have crystallized in their well-known equilibrium structures and the relative orientation of the formed crystallites is such that the LMAes of the molecules are arranged parallel. The defocused image in the inset shows the real image of the diffracting area (bright circle) revealing nearly parallel aligned needles. The bright field image depicted in the middle of the left column shows the morphology of the 1-cycle sample in higher magnification. When compared with the well-studied morphology of *p*-6P needles, here additionally needle-like structures are evident which exhibit strong contrast, appearing nearly black. The strongly enhanced contrast points towards height differences with respect to the underlying needle-structures. To prove this assumption, rotational tilt was performed; the figure at the bottom left corner shows the morphology of the sample tilted by 35°. It reveals that structures growing on top are significantly larger than the underlying needle-like structures. In this two-layer system (one cycle) α-6T molecules are deposited on top of a *p*-6P layer; hence these unusual wall-like morphologies correspond to α-6T crystallites. These wall-like structures appear to be flexibly bendable rather than rigid which could be also an

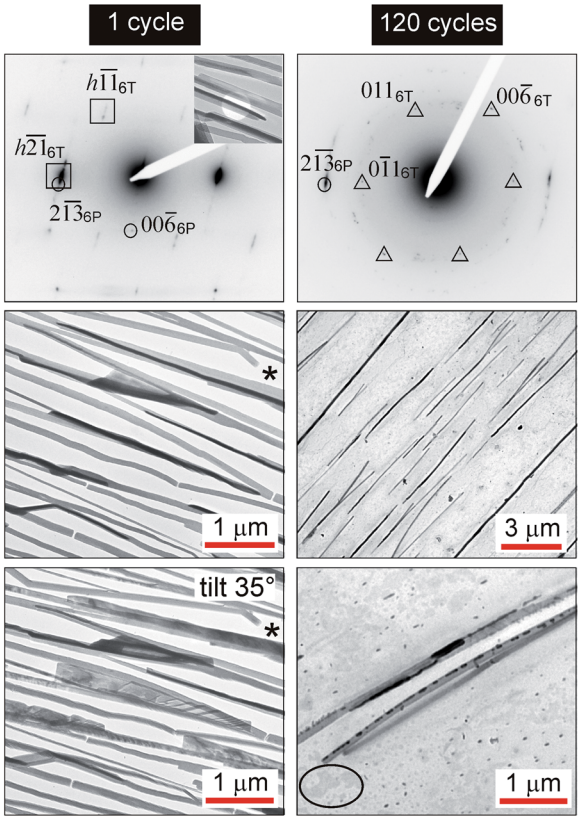

Fig. 6 The left column shows TEM results obtained for a 1-cycle sample. A typical electron diffraction pattern is depicted at the top. The bright field image in the middle shows the typical morphology. Below, the same area tilted along the long needle axis by 35° is shown. Asterisks denote the same area on the sample. The right column depicts TEM results measured for a 120-cycle sample. At the top a typical electron diffraction pattern is shown. In the middle the corresponding bright field image is depicted. On the bottom right higher magnification of the observed needle-like structures is shown. Reflexes are denoted according to Fig. 4.

explanation for the often found variations in the diffraction patterns assigned to α-6T crystallites of lying molecules.

The multilayer heterostructure shown in the right column of Fig. 6 is prepared by 120 deposition cycles, where the nominal thicknesses of the single *p*-6P and α-6T layers are 0.8 nm and 3.4 nm, respectively. The typical diffraction pattern shown at the top is a superposition of different diffraction patterns making the assignment to specific orientations of the involved crystallites increasingly difficult. Contributions from *p*-6P($11\bar{1}$) and α-6T(100) crystallites are indicated by circles and triangles, respectively. Other diffraction spots, most probably due to α-6T($\bar{4}11$) crystallites, cannot be assigned unambiguously. However, the bright field image shown in the middle reveals that the deposited molecules still arrange in rather parallel and long needles. Also here, the morphology with enhanced contrast is present and indicates wall-like morphologies. In contrast to the previously discussed 1-cycle sample, for the 120-cycle sample α-6T(100) diffraction patterns corresponding to upright standing α-6T molecules are more often observed. Consistently, in the bright field images additional features beside the needle like-structures are present. Beside the small nuclei which are reminiscent of the elongated islands observed for *p*-6P in the monolayer regime (*cf.* Fig. 2), we observe flat islands with low contrast – a morphology typical for crystallites of upright standing α-6T molecules (see the encircled area in the bottom right corner). This finding suggests that fast deposition cycles render the crystallization of α-6T in islands of upright-standing molecules more favourable. This orientation is preferentially found on substrates exhibiting weak interaction with the deposited molecules.[4,45]

For a better discrimination of domains containing *p*-6P and α-6T molecules, respectively, a *cross-sectional* TEM measurement with a combined Auger electron spectroscopy of a 10-cycle sample was performed (Fig. 7). In the HR-TEM image shown in Fig. 7a two different regions can be distinguished (the white arrow indicates the growth direction): in the lower part as well as on the left side regions with periodic modulation of intensity are visible, which crystalline lattice planes; in contrast, the triangular inclusion in the middle does not show any periodic structures. A FFT analysis of the region showing periodic modulation yields a periodicity of 2.8 nm, which is in good agreement with the lattice spacing d_{001} of the *p*-6P crystal structure (compare Fig. 3b). This suggests phase separation: regions showing periodicities correspond to *p*-6P($11\bar{1}$) crystallites while most probably a region containing α-6T molecules is visible in the middle of the image. To substantiate this assumption Auger electron spectroscopy was measured (Fig. 7b). Here, blue lines

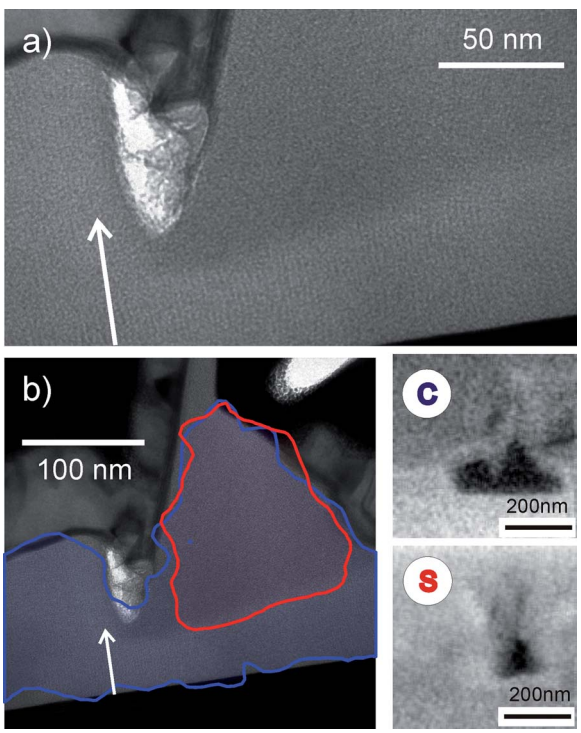

Fig. 7 (a) *Cross-sectional* transmission electron microscopy (TEM) image of a α-6T–*p*-6P multilayer heterostructure prepared by 10 deposition cycles (the white area in the image is caused by a hole in the sample). The white arrow indicates the growth direction. (b) TEM image with overlaid isointensities measured by Auger electron spectroscopy: carbon (blue) and sulphur (red). Again, the white arrow indicates the growth direction. On the right side images for carbon and sulphur rich domains, respectively, are shown.

correspond to regions where signals from carbon are detected and red lines denote the presence of sulfur atoms (and hence α-6T molecules). In regions showing periodicity in the HR-TEM image (Fig. 7a) indeed only carbon atoms are measured, corroborating that pure *p*-6P(11$\bar{1}$) crystallites have formed. In contrast, the triangular structure in the middle additionally contains sulfur atoms, indicating the presence of α-6T molecules. However, the image in Fig. 7a does not allow us to deduce the crystal structure present in the region without periodic contrast modulation. Therefore, we cannot conclude whether in this region solely α-6T molecules crystallize in their equilibrium structure, as measured for the 1 cycle sample, or if mixed crystals form.

In conclusion, for the 10 and 120-cycle samples in (cross-sectional) TEM we clearly observe *p*-6P crystallites oriented with the (11$\bar{1}$) lattice plane parallel to the substrate surface as well as α-6T molecules crystallizing in the low temperature phase with the (100) contact plane. However, to corroborate that the α-6T molecules still arrange in ($\bar{4}$11) oriented crystallites with their LMAes parallel to those of *p*-6P molecules (as the bright field images in the right column of Fig. 6 suggest), complementary XRD measurements are required.

3.2.2 XRD reciprocal space maps. Fig. 8a shows XRD specular scans for the periodically grown α-6T–*p*-6P heterostructures summarized in Table 1. Measured Bragg peaks indicate lattice planes parallel to the substrate surface. The 0-cycle sample is a pure *p*-6P thin film consisting of a 33 nm thick *p*-6P template layer and one *p*-6P layer (98.1 nm) on top. A peak at $q_z = 1.383$ Å^{-1} is measured in addition to the (004) peak of the muscovite mica substrate ($q_z = 1.26$ Å^{-1}). It can be assigned to the *p*-6P(11$\bar{1}$) lattice plane of the β-phase with the lattice spacing measured at $d_{11\bar{1}} = 4.57 \pm 0.01$ Å. In the specular scan of a 1-cycle sample (additional deposition of a 405 nm thick α-6T layer) a new peak at $q_z = 1.420$ Å^{-1} appears which is attributed to the ($\bar{4}$11) lattice plane of a α-6T low temperature phase measured at $d_{\bar{4}11} = 4.42 \pm 0.01$ Å. These measurements confirm the orientations observed by TEM/TED measurements very well (*cf.* Fig. 6). More interestingly, specular scans reveal that the α-6T($\bar{4}$11) orientation is present for all observed films, even those prepared by 120 deposition cycles. However, the α-6T(100) orientation which was observed in TED (Fig. 6, right column at the top) is not present in the specular scan. The corresponding α-6T islands grow between the needle-like structures (Fig. 6, right column, middle and bottom) and their scattering volume is too small for detection with XRD as opposed to the locally more sensitive ED.

To examine how the mosaicity, *i.e.* degree of crystalline order parallel to the substrate surface, depends on the number of deposition cycles X-ray diffraction reciprocal space maps (RSMs) were measured (for details, see the Experimental section) and are summarized in Fig. 8b. The peaks measured in the RSM for the 0-cycle sample can be assigned to the (004) peak of the muscovite mica substrate and the (11$\bar{1}$) peak of *p*-6P (upper left corner of Fig. 8b). The corresponding rocking curve of the *p*-6P(11$\bar{1}$) peak yields a rocking width of 0.5°, a rather small value for organic thin films which indicates highly oriented crystallites. For the 1-cycle sample the position and the rocking width of *p*-6P(11$\bar{1}$) remains constant and an additional α-6T($\bar{4}$11) peak appears. The latter exhibits a rocking width of 1.4° which is significantly larger than for *p*-6P crystallites but is still indicative of well-aligned crystallites. With the increasing number of cycles, the mosaicity of *p*-6P crystallites only slightly increases, reaching a value of 0.7° for the 120 cycle sample. In contrast, the mosaicity of α-6T crystallites strongly increases reaching a value of approx. 4 for 120 cycles.

Further, it is observed that the alternate deposition affects the position of the peaks as well. The positions of the muscovite mica(004) and *p*-6P(11$\bar{1}$) peaks basically remain constant when the number of deposition cycles is increased. In contrast, the position of maximum intensity assigned to the α-6T($\bar{4}$11) peak increasingly deviates from its literature value ($d_{\bar{4}11} = 4.4213$ Å), with the largest difference amounting to $d_{\bar{4}11} = 0.05$ Å for 120 cycles. This trend is clearly visible in the specular scan (dashed line in Fig. 8a). The change of the α-6T($\bar{4}$11) lattice spacing is

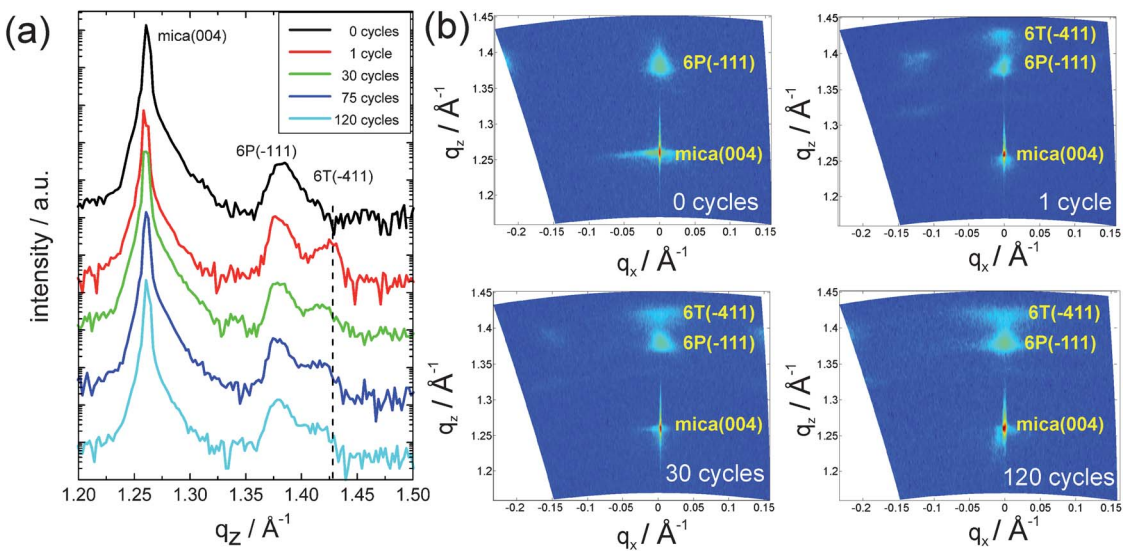

Fig. 8 (a) X-ray diffraction specular scans of periodically grown α-6T–*p*-6P layered heterostructures (0, 1, 30, 75 and 120 cycles). (b) Corresponding X-ray diffraction reciprocal space maps for samples grown with 0, 1, 30 and 120 cycles.

rather continuous as is seen best in the RSM of the 120-cycle sample (Fig. 8b, bottom right panel), where the corresponding Bragg peak appears considerably broadened.

3.2.3 XRD pole figure measurements. In contrast to specular scans, which probe lattice planes oriented parallel to the substrate surface, pole figure measurements give information on the orientation distribution of all lattice planes with a finite structure factor. This enables an efficient determination of the actual crystal structures as well as of the epitaxial relationship between involved crystallites. As the herring-bone arrangement of *p*-6P and α-6T molecules in the corresponding crystal structures is rather similar, most of the high intensity lattice planes are at the identical scattering angle and pole direction. Therefore, for measuring the pole figure lattice spacings were chosen in a way such that detectable diffraction intensity is present exclusively for one of the two crystal structures: $d_{006} = 4.33$ Å for *p*-6P crystallites ($q = 1.424$ Å^{-1}) and $d_{12.00} = 3.73$ Å for α-6T crystallites ($q = 1.687$ Å^{-1}) enables distinguishing between contributions from the two molecular species. Pole figures of a one-cycle sample measured for *p*-6P (d_{006}) and α-6T ($d_{12.00}$) are shown in Fig. 9a and b, respectively. The measured enhanced pole densities (EPDs) marked with red crosses stem from the muscovite mica(001) substrate. In Fig. 9a EPDs that are not due to muscovite mica can be assigned to the β-phase of *p*-6P assuming the $(11\bar{1})/(\bar{1}\bar{1}1)$ lattice planes to be parallel to the substrate surface. In total, there are four domains: two domains mirrored with respect to each other (corresponding to the $11\bar{1}$ and $\bar{1}\bar{1}1$ contact plane, respectively) and the corresponding domains rotated by 180°. As these four domains lie close to each other, in Fig. 9 only two mirrored domains are indexed, whereas the indexation of the domains rotated by 180° and their corresponding LMAs are not depicted here. Measured reflexion spots are rather narrow indicating that the in-plane order of *p*-6P crystallites is well defined. Furthermore, the epitaxial alignment of the *p*-6P molecules with respect to the muscovite mica substrate can be derived: we observe that the long molecular axis (LMA) of *p*-6P encloses an angle of 82° ± 2° with the [110] direction of the muscovite mica substrate. This finding is in line with the previously observed behaviour of *p*-6P molecules on muscovite mica substrates.[13] The pole figure measured for the (12.00) lattice plane of α-6T is shown in panel b and can be interpreted as the low temperature phase of α-6T with the $(\bar{4}11)/(4\bar{1}\bar{1})$ lattice planes parallel to the substrate surface and the corresponding domains rotated by 180°. The rather sharp EPDs are again indicative of well-aligned domains. Further, as the arrows in the corresponding pole figures indicate, the LMA of α-6T molecules is oriented exactly parallel to the LMA of *p*-6P.

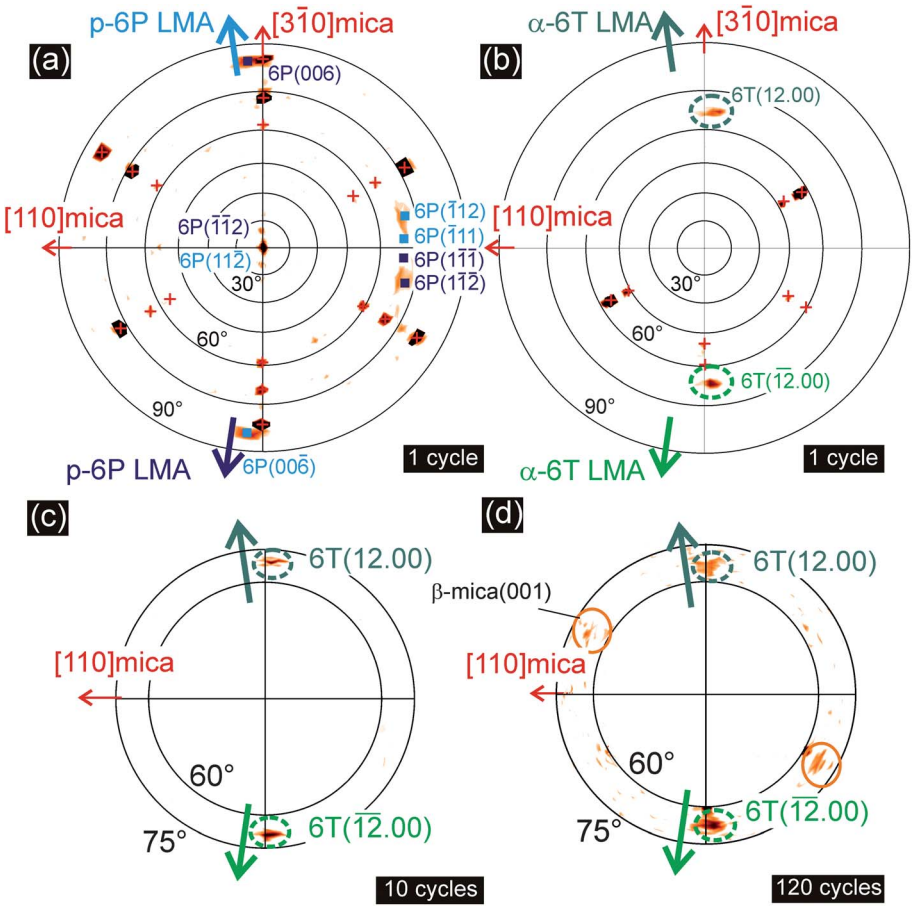

Fig. 9 X-ray diffraction pole figure measurements performed for: (a) one-cycle sample for the 6P(006) reflex ($q = 1.424$ Å^{-1}), (b) one-cycle sample for the 6T(12.00) reflex ($q = 1.687$ Å^{-1}), (c) 10-cycle sample for the 6T(12.00) reflex and (d) 120-cycle sample for the 6T(12.00) reflex. Arrows indicate the azimuthal orientation of the corresponding long molecular axes (LMAs). Red crosses denote peaks due to the muscovite mica substrate.

This means they have arranged parallel adopting the same orientation of their herring bone packing as was also observed in the TEM/TED measurements (see Fig. 4). This alignment, which is advantageous for optical applications, is preserved even for large numbers of deposition cycles as shown for 10 and 120 cycles in Fig. 9c and d. For both pole figures only the relevant range $\psi = 60-75^\circ$ of the 6T(12.00) pole figure is depicted, as the orientation of the muscovite mica substrate is the same as in the case of panel b and that of *p*-6P crystallites the same as in panel a. The azimuthal alignment of the α-6T crystallites is identical to the one-cycle sample which can be explained by the low temperature phase. We mention for the sake of completeness that muscovite mica (001) exhibits two cleavage planes which are identical but azimuthally rotated by 120° with respect to each other: α-muscovite mica(001) and β-muscovite mica(001) surfaces.[13] Upon cleavage of the substrate surface terraces can form. In this case both muscovite mica surfaces are present simultaneously, explaining the additionally occurring EPDs encircled by orange circles in the lower part of Fig. 9d (the β-muscovite mica(001) surface) which do not obey the symmetry imposed by the α-muscovite mica(001) surface. The EPDs discussed above correspond to crystallites formed on the α-muscovite mica(001) surface.

Summarizing, pole figure measurements (Fig. 9) reveal that even for large numbers of deposition cycles *p*-6P and α-6T molecules phase separate, each forming their equilibrium crystal structure. Hence, the slight change of α-6T $d_{\bar{4}11}$ lattice spacing observed in the specular scan (Fig. 8) does not correspond to a formation of a mixed phase. Most probably this change originates from the strain formed upon the adaptation of α-6T crystallites to the herring-bone structure of *p*-6P: an in-plane lattice spacing contraction (of 6T $d_{3\bar{2}\bar{1}}$ =3.217 Å to fit *p*-6P $d_{2\bar{1}\bar{3}}$ =3.116 Å) leads to an expansion perpendicular to the substrate surface (*i.e.* α-6T $d_{\bar{4}11}$).

4 Conclusions

We have shown that *p*-6P alignment layers of less than 2 nm thickness induce epitaxial alignment of subsequently deposited α-6T molecules. The α-6T crystallites grow preferentially with the $(\bar{4}11)$ lattice plane of the low temperature phase parallel to the substrate surface. The molecules of α-6T crystallites align with their LMAs parallel to those of *p*-6P crystallites and the relative in-plane orientation leads to a perfect adoption of their herring-bone structures. For periodically deposited α-6T–*p*-6P heterostructures it is important to clarify: (a) is the azimuthal alignment of the α-6T–*p*-6P crystallites preserved, (b) does the number of deposition cycles affect the azimuthal alignment of the evolved crystallites and (c) do the formed crystal structures correspond to the equilibrium structures of *p*-6P and α-6T molecules found in bi-layer systems or do they mix on a molecular level forming solid solutions? TEM and TED measurements with combined Auger electron spectroscopy show that in addition to domains containing α-6T molecules, pure *p*-6P$(11\bar{1})$ crystallites form. Using an XRD specular scan and pole figure measurements we could clarify that for all periodically deposited heterostructures phase separated crystallization occurs and that the molecules crystallize in their respective equilibrium structures. In addition to *p*-6P$(11\bar{1})$ crystallites also α-6T$(\bar{4}11)$ crystallites form and, independently of the number of deposition cycles, the relative azimuthal alignment found in the bilayer system is preserved. The only structural change we observe is a slight adaptation of lattice spacings of the α-6T crystallites to those of *p*-6P. The consequence is a coexistence of strained and strain free α-6T crystallites, where the latter show a significantly larger mosaicity.

In contrast to the system of co-evaporated α-6T–*p*-6P molecules,[35] for periodically deposited α-6T–*p*-6P heterostructures no indication for phase mixing is found. This can be rationalized by the difference in the preparation technique of the periodically deposited α-6T–*p*-6P compared to the co-evaporated systems. First, the molecules are deposited alternately and not simultaneously as in the case of co-evaporation. Second, the evaporation technique of hot wall epitaxy used here operates close to the thermodynamic equilibrium. Both aspects facilitate a crystallization of the molecules in their equilibrium structures. As opposed to this, in co-evaporated films, mixing occurs because of kinetic reasons during growth and may therefore lead to "kinetically trapped" metastable phases. Furthermore, contrary to co-evaporated structures, alternate deposition of α-6T and *p*-6P molecules results in highly anisotropic, needle-like structures with a well-defined epitaxial in-plane order that is highly favourable for optically active thin films.

Acknowledgements

This work was supported by the Austrian Science Fund (FWF): [P21094], Land Oberösterreich, Projekt "Organische Nanostrukturen".

References

1 G. Leising, S. Tasch, F. Meghdadi, L. Athouel, G. Froyer and U. Scherf, *Synth. Met.*, 1996, **81**, 185–189.
2 T. Noda, H. Ogawa, N. Noma and Y. Shirota, *J. Mater. Chem.*, 1999, **9**, 2177–2181.
3 T. Mikami and H. Yanagi, *Appl. Phys. Lett.*, 1998, **73**, 563.
4 B. Servet, G. Horowitz, S. Ries, O. Lagorsse, P. Alnot, A. Yassar, F. Deloffre, P. Srivastava and R. Hajlaoui, *Chem. Mater.*, 1994, **6**, 1809–1815.
5 G. Horowitz, B. Bachet, A. Yassar, P. Lang, F. Demanze, J. Fave and F. Garnier, *Chem. Mater.*, 1995, **7**, 1337–1341.
6 H. E. Katz, *J. Mater. Chem.*, 1997, **7**, 369–376.
7 F. Balzer, J. Beermann, S. I. Bozhevolnyi, A. C. Simonsen and H. Rubahn, *Nano Lett.*, 2003, **3**, 1311–1314.
8 P. Puschnig and C. Ambrosch-Draxl, *Phys. Rev. B: Condens. Matter*, 1999, **60**, 7891–7898.
9 C. Simbrunner, D. Nabok, G. Hernandez-Sosa, M. Oehzelt, T. Djuric, R. Resel, L. Romaner, P. Puschnig, C. Ambrosch-Draxl, I. Salzmann, G. Schwabegger, I. Watzinger and H. Sitter, *J. Am. Chem. Soc.*, 2011, **133**, 3056–3062.
10 H. Plank, R. Resel, H. Sitter, A. Andreev, N. Sariciftci, G. Hlawacek, C. Teichert, A. Thierry and B. Lotz, *Thin Solid Films*, 2003, **443**, 108–114.
11 S. Müllegger and A. Winkler, *Surf. Sci.*, 2006, **600**, 1290–1299.
12 F. Balzer and H. Rubahn, *Appl. Phys. Lett.*, 2001, **79**, 3860.
13 R. Resel, T. Haber, O. Lengyel, H. Sitter, F. Balzer and H. Rubahn, *Surf. Interface Anal.*, 2009, **41**, 764–770.
14 A. Piaggi, G. Lanzani, G. Bongiovanni, A. Mura, W. Graupner, F. Meghdadi, G. Leising and M. Nisoli, *Phys. Rev. B: Condens. Matter*, 1997, **56**, 10133–10137.
15 F. Quochi, *J. Opt.*, 2010, **12**, 024003.
16 F. Balzer and H. Rubahn, *Adv. Funct. Mater.*, 2005, **15**, 17–24.
17 F. Biscarini, R. Zamboni, P. Samor, P. Ostoja and C. Taliani, *Phys. Rev. B: Condens. Matter*, 1995, **52**, 14868–14877.
18 L. Kankate, F. Balzer, H. Niehus and H. Rubahn, *Thin Solid Films*, 2009, **518**, 130–137.

19 P. Viville, R. Lazzaroni, J. LucBrdas, P. Moretti, P. Samor and F. Biscarini, *Adv. Mater.*, 1998, **10**, 57–60.
20 C. Simbrunner, G. Hernandez-Sosa, M. Oehzelt, T. Djuric, I. Salzmann, M. Brinkmann, G. Schwabegger, I. Watzinger, H. Sitter and R. Resel, *Phys. Rev. B: Condens. Matter Mater. Phys.*, 2011, **83**, 115443.
21 M. Campione, L. Raimondo, M. Moret, P. Campiglio, E. Fumagalli and A. Sassella, *Chem. Mater.*, 2009, **21**, 4859–4867.
22 S. Mannsfeld, K. Leo and T. Fritz, *Phys. Rev. Lett.*, 2005, **94**.
23 M. Moret, A. Borghesi, M. Campione, E. Fumagalli, L. Raimondo and A. Sassella, *Cryst. Res. Technol.*, 2011, **46**, 827–832.
24 G. Koller, S. Berkebile, J. R. Krenn, F. P. Netzer, M. Oehzelt, T. Haber, R. Resel and M. G. Ramsey, *Nano Lett.*, 2006, **6**, 1207–1212.
25 C. Simbrunner, F. Quochi, G. Hernandez-Sosa, M. Oehzelt, R. Resel, G. Hesser, M. Arndt, M. Saba, A. Mura, G. Bongiovanni and H. Sitter, *ACS Nano*, 2010, **4**, 6244–6250.
26 C. Simbrunner, G. Hernandez-Sosa, F. Quochi, G. Schwabegger, C. Botta, M. Oehzelt, I. Salzmann, T. Djuric, A. Neuhold, R. Resel, M. Saba, A. Mura, G. Bongiovanni, A. Vollmer, N. Koch and H. Sitter, *ACS Nano*, 2012, **6**, 4629–4639.
27 A. Hinderhofer, C. Frank, T. Hosokai, A. Resta, A. Gerlach and F. Schreiber, *J. Chem. Phys.*, 2011, **134**, 104702.
28 R. Jones, *Soft Condensed Matter*, Oxford University Press, Oxford, 2002.
29 S. Stlen, *Chemical Thermodynamics of Materials: Macroscopic and Microscopic Aspects*, J. Wiley, Hoboken NJ, 2004.
30 I. Salzmann, S. Duhm, G. Heimel, M. Oehzelt, R. Kniprath, R. L. Johnson, J. P. Rabe and N. Koch, *J. Am. Chem. Soc.*, 2008, **130**, 12870–12871.
31 I. Salzmann, S. Duhm, G. Heimel, J. P. Rabe, N. Koch, M. Oehzelt, Y. Sakamoto and T. Suzuki, *Langmuir*, 2008, **24**, 7294–7298.
32 W. D. Callister, *Materials Science and Engineering: An Introduction*, John Wiley & Sons, New York, 2007.
33 L. Vegard, *Z. Phys.*, 1931, **71**, 465–472.
34 K. Baker, A. Fratini, T. Resch, H. Knachel, W. Adams, E. Socci and B. Farmer, *Polymer*, 1993, **34**, 1571–1587.
35 J. Vogel, I. Salzmann, S. Duhm, M. Oehzelt, J. P. Rabe and N. Koch, *J. Mater. Chem.*, 2010, **20**, 4055.
36 W. Kraus and G. Nolzeb, *J. Appl. Crystallogr.*, 1996, **29**, 301–303.
37 I. Salzmann and R. Resel, *J. Appl. Crystallogr.*, 2004, **37**, 1029–1033.
38 L. Kankate, F. Balzer, H. Niehus and H. Rubahn, *J. Chem. Phys.*, 2008, **128**, 084709.
39 P. Leclre, M. Surin, P. Viville, R. Lazzaroni, A. F. M. Kilbinger, O. Henze, W. J. Feast, M. Cavallini, F. Biscarini, A. P. H. J. Schenning and E. W. Meijer, *Chem. Mater.*, 2004, **16**, 4452–4466.
40 L. Dissado and A. Mau, *Chem. Phys. Lett.*, 1975, **31**, 588–592.
41 C. A. Hutchison and B. W. Mangum, *J. Chem. Phys.*, 1961, **34**, 908.
42 L. Sacconi, M. Ciampolini and G. Speroni, *J. Am. Chem. Soc.*, 1965, **87**, 3102–3106.
43 D. Braga, F. Grepioni, L. Maini, M. Polito, K. Rubini, M. Chierotti and R. Gobetto, *Chem.–Eur. J.*, 2009, **15**, 1508–1515.
44 M. Vaida, L. J. W. Shimon, Y. Weisinger-Lewin, F. Frolow, M. Lahav, L. Leiserowitz and R. K. Mcmullan, *Science*, 1988, **241**, 1475–1479.
45 G. Hernandez-Sosa, C. Simbrunner, T. Höfler, A. Moser, O. Werzer, B. Kunert, G. Trimmel, W. Kern, R. Resel and H. Sitter, *Org. Electron.*, 2009, **10**, 326–332.